

Supplementary Material

Feldspar alteration by disequilibrium CO₂-H₂O fluids in reservoir sandstones: Implications for CCS

Authors: Natalie Farrell, Lining Yang, Mike Flowerdew, Chris Mark, Buhari Ardo, Kevin Taylor, Nico Bigaroni, Mick Pointon, Lewis Hughes, John Waters, Lee Paul

S1. METHODS

S1.1. Experiment duration compared to geological timescales

Temperature exerts a strong influence on reaction rates, typically doubling the rate for every 10°C increase (Hall, 2015). Consequently, the six-day duration of our experimentally induced reactions corresponds to rates hundreds to thousands of times faster than those expected under reservoir conditions. To quantify this, we applied the Arrhenius equation to calculate reaction rate ratios and extrapolate the K-feldspar dissolution times observed in experiments conducted at 400°C and 550°C to the in situ reservoir temperature of 80°C. Calculations used two different activation energies for K-feldspar dissolution: 50 kJ/mol, reported by Blum and Stillings (1995) for dissolution in acidic conditions (pH ~3), and 38 kJ/mol, from Helgeson (1984) for dissolution under neutral pH conditions. Based on these activation energies, the K-feldspar dissolution observed at 400°C would translate to reaction times between approximately 7.7 and 53 years under reservoir conditions, indicating that the experiments proceed roughly 470 to 3300 times faster. Similarly, reactions observed at 550°C correspond to 26.6 to 274 years in situ, representing rates accelerated by factors of about 1600 to 16,000.

These calculations serve as a basic guide to assess the experimental results' relevance but do not account for additional rate-limiting or rate-enhancing factors, most notably the role of intergranular stresses in accelerating reaction rates. Nonetheless, these estimates suggest that the effects of K-feldspar dissolution could become significant within a CCS reservoir over human timescales.

S1.2. Experimental apparatus

Experiments were conducted using externally heated triaxial deformation apparatus, 'Nimonic 2' and 'Nimonic 3' (see main text for methodology).

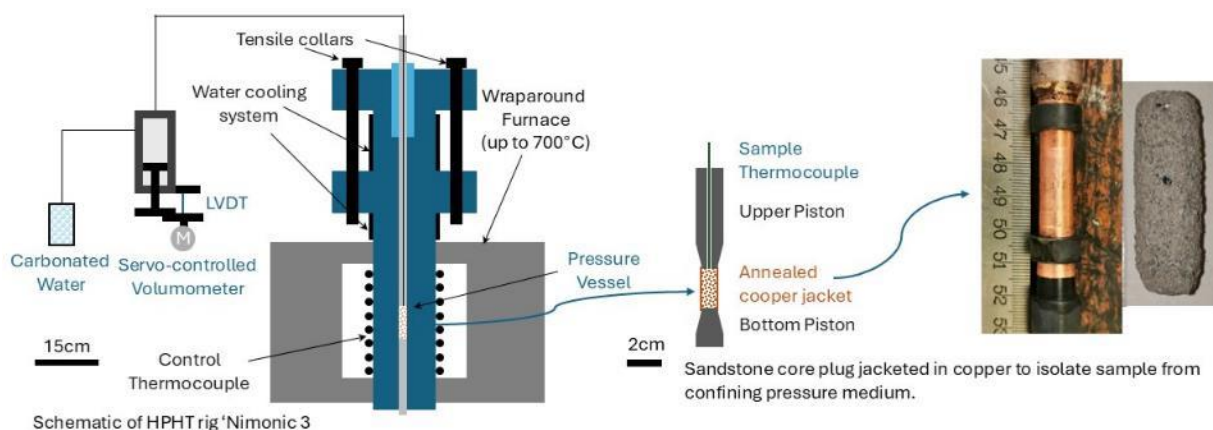


Figure S1. Schematic cross section diagram of high pressure, high temperature triaxial rig 'Nimonic 3' illustrating the sample assembly within the Nimonic pistons (rhs), confinement of sample with the pressure vessel and furnace (centre) and pore volumometer controlling injection and pressure of pore fluid along the top piston (lhs).

Tap water was used as the pore fluid for initial equilibration of the rock samples. This choice was intentional: rather than using deionised water, which is chemically undersaturated and can promote artificial mineral dissolution. The goal was to minimise the role of the water itself as a reactive agent during the saturation stage and better mimic natural formation fluids, which would typically be in partial equilibrium with the reservoir rock. By pre-equilibrating the water:rock system, we aimed to isolate and better assess the specific effects of CO₂-enriched fluids on mineral solubility and reactivity, rather than capturing reactions driven primarily by fluid disequilibrium.

Element	Symbol	Concentration (ppb)	Comparison to UK drinking water standards
Aluminium	Al	13	Below normal range
Iron	Fe	4.8	Very low
Zinc	Zn	21	Very low
Copper	Cu	6.7	Normal, very low
Lead	Pb	0.1	Normal very low
Arsenic	As	0.4	Very low
Calcium	Ca	4537	Normal, very low
Magnesium	Mg	1155	Below normal range
Sodium	Na	5792	Normal
Potassium	K	444	Below normal range

Table S1. Pore fluid chemistry of tap water used as pore fluid in reaction experiments analysed using ICP-MS

S1.3. XRD method

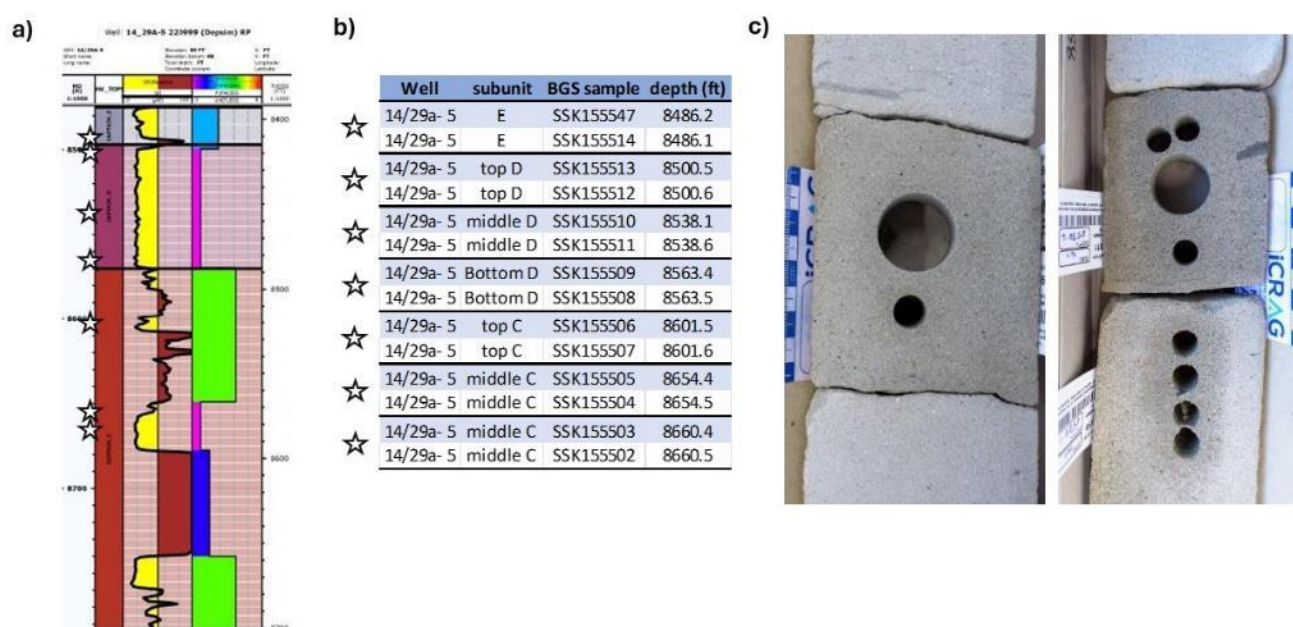
Measurements were carried out on a Bruker D2 Phaser diffractometer, equipped with a Lynxeye XE-T detector with an axial 2.5° Soller slit and anti-scatter screen. The X-ray generator was set to 30kV and 10mA, powering an X-ray tube with a copper source, providing CuK_{α1} X-rays with a wavelength of 1.5406Å. Sample preparation involved grinding ~0.1g

46 sample material, mixed with ~1ml of amyl acetate, using a pestle and mortar. The resultant slurries
 47 were transferred to glass microscope slides and air dried.

48 Sample were scanned from 5-70°2θ, with a step size of 0.04 ° and a count time of 0.4s per step. The
 49 resultant patterns were evaluated using EVA version 5, which compares experimental data to standards
 50 from the ICDD (International Centre for Diffraction Data) Database.

51 S2. MATERIALS

52 Samples were collected from well 14/29a-5 at a range of depths from sandstone units defined as C, D
 53 and E at depths listed in Figure 2.a and linked to wireline log data from the wellbore 2.b (Shell
 54 Geochemical Reactivity Report, 2015). Mineral composition was determined for all samples using X-
 55 ray diffraction analysis (Table 1).



56 Figure S2. Sampling locations from well core. At each sample site 20mm diameter cores were plugged for provenance
 57 and images analysis and at 'D sand middle' and 'D sand top' 10 mm diameter cores were plugged for experiments
 58 (c).

Minerals	Wt% Rietveld						
	C sand' massive	C sand' laminated	C sand' cemented	D sand' base	D sand' middle	D sand' top	E sand'
Albite	7.6	10.3	0.2	2.4	8.1	6.4	4.6
Glauconite	0.1	0.8	0.7	1.1	1.1	0.0	0.2
Calcite	1.0	1.1	0.7	0.4	0.7	0.3	1.1
Kaolinite	4.0	9.0	3.1	0.5	7.7	5.8	8.0
Microcline	7.0	9.1	6.7	7.0	8.7	3.8	5.1
Quartz	80.3	69.6	86.7	88.6	73.0	83.6	81.0
Halite					0.8		
Augite Px			2.0				

59

60 **Table S2. Mineral composition for all Captain Sandstone Formation sandstone units derived from XRD analysis.**
61 Due to limitation on the amount of rock that could be sampled we used core plugs from the middle and
62 top of the D sand unit in experiments. Sample mineralogy from ‘D middle’ comprised 73% quartz,
63 **8.1% plagioclase, 8.7% K-feldspar, 7.7% kaolinite**, 1.1% glauconite, 0.7% calcite, 0.8% halite.
64 Sample mineralogy from ‘D top’ contained 83.6% quartz, **6.4% plagioclase, 3.8% K-feldspar, 5.8%**
65 **kaolinite**, 0.35% calcite (Table 1). Microstructural analysis of D middle and D top showed the D
66 middle had more pore area 39% compared to D top 24.4% possible indicating higher porosities in the
67 D middle samples.

68 S2.1. MICROSTRUCTURAL IMAGES

69 The following images show additional examples of mineral textures from BSE images (see main text
70 for methodology) of pre experiment samples (Figure 3- 4) and post experiment samples (Figures 3-12)

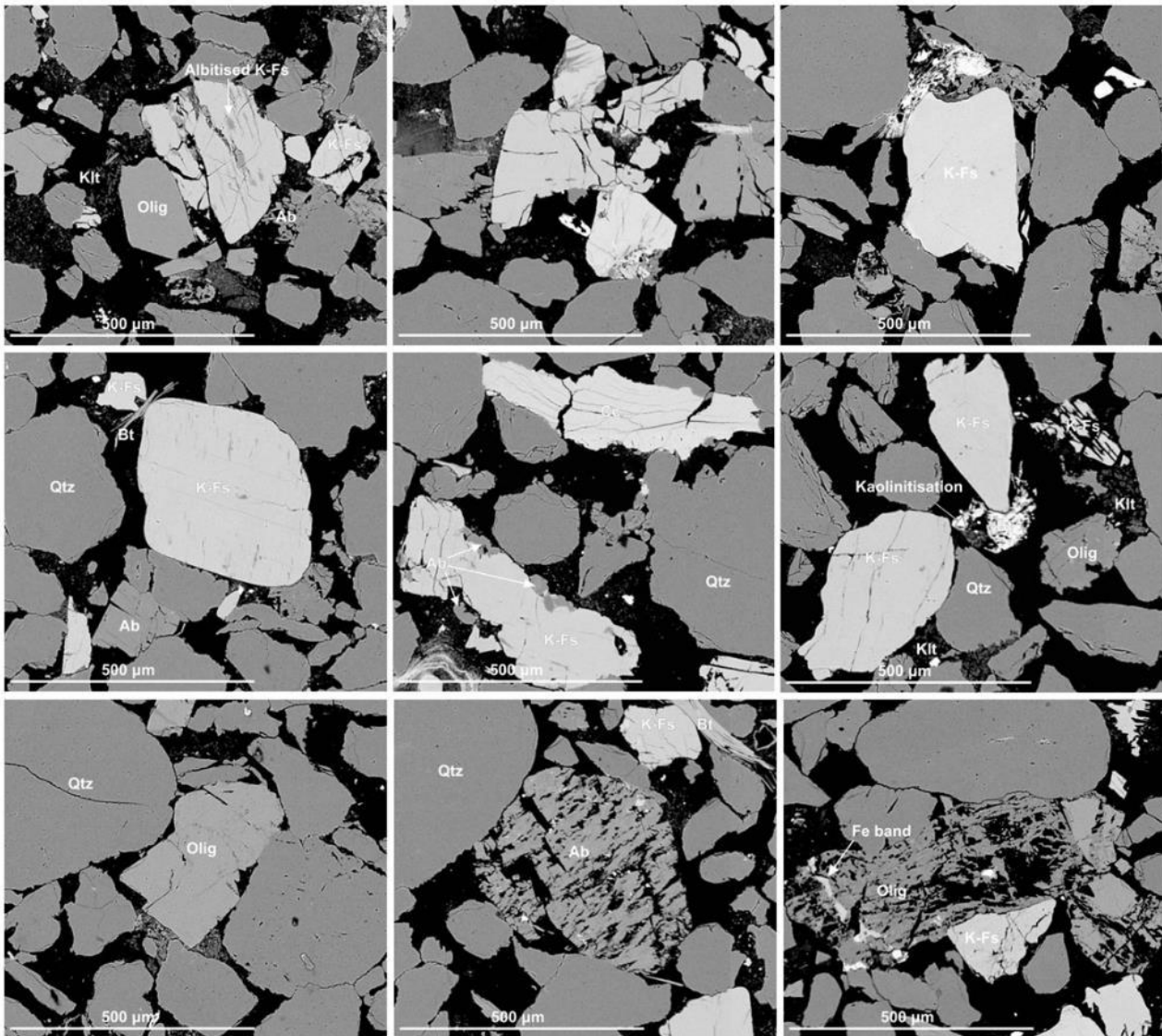


Figure S3. BSE images of feldspars in pre-experiment sandstone. Textures include pre-reaction K-feldspars with albitised lamellae and randomly oriented, curvilinear intergranular fractures related to crushing. Also shown are blocky, intact oligoclase grains and large skeletal albite grains with coherent grain boundaries. Abbreviations follow Whitney and Evans (2010).

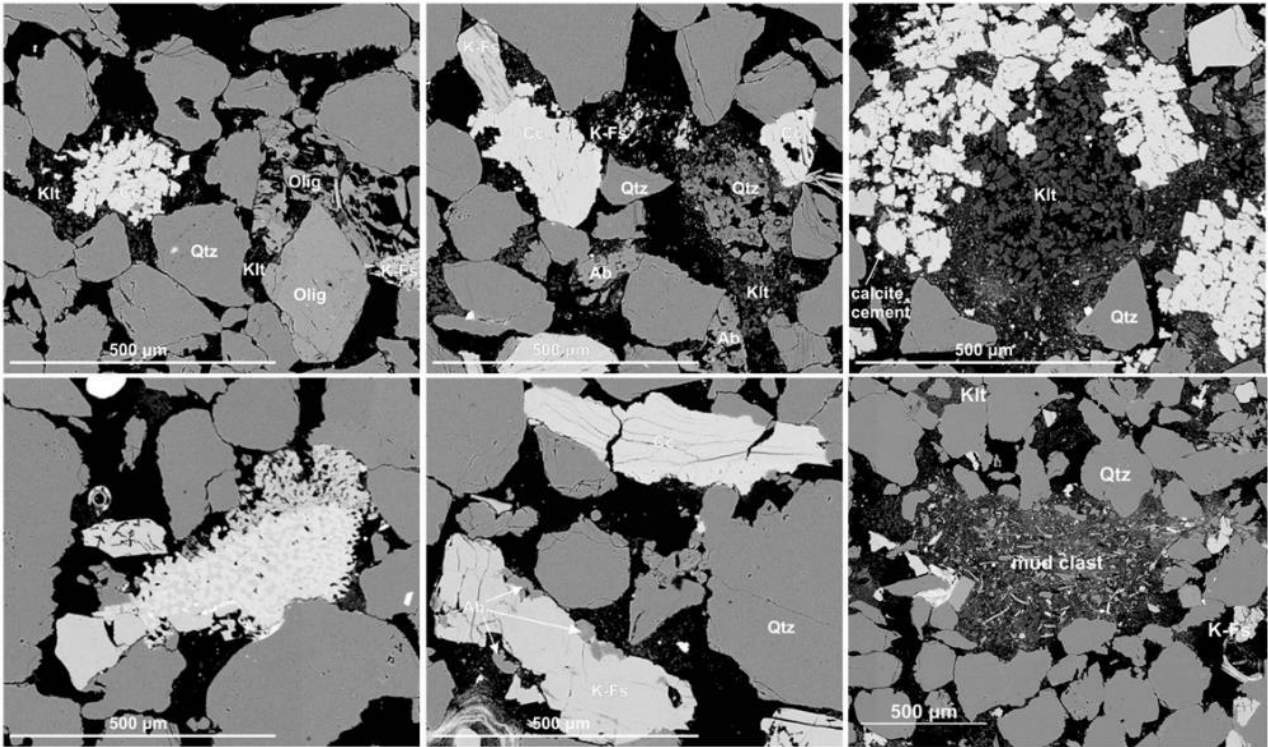


Fig S4. BSE images of calcite patches, grains, and clays in pre-experiment D sands. Features include patchy calcite associated with well-formed kaolinite patches and mud clasts containing mixed 1:1 clays.

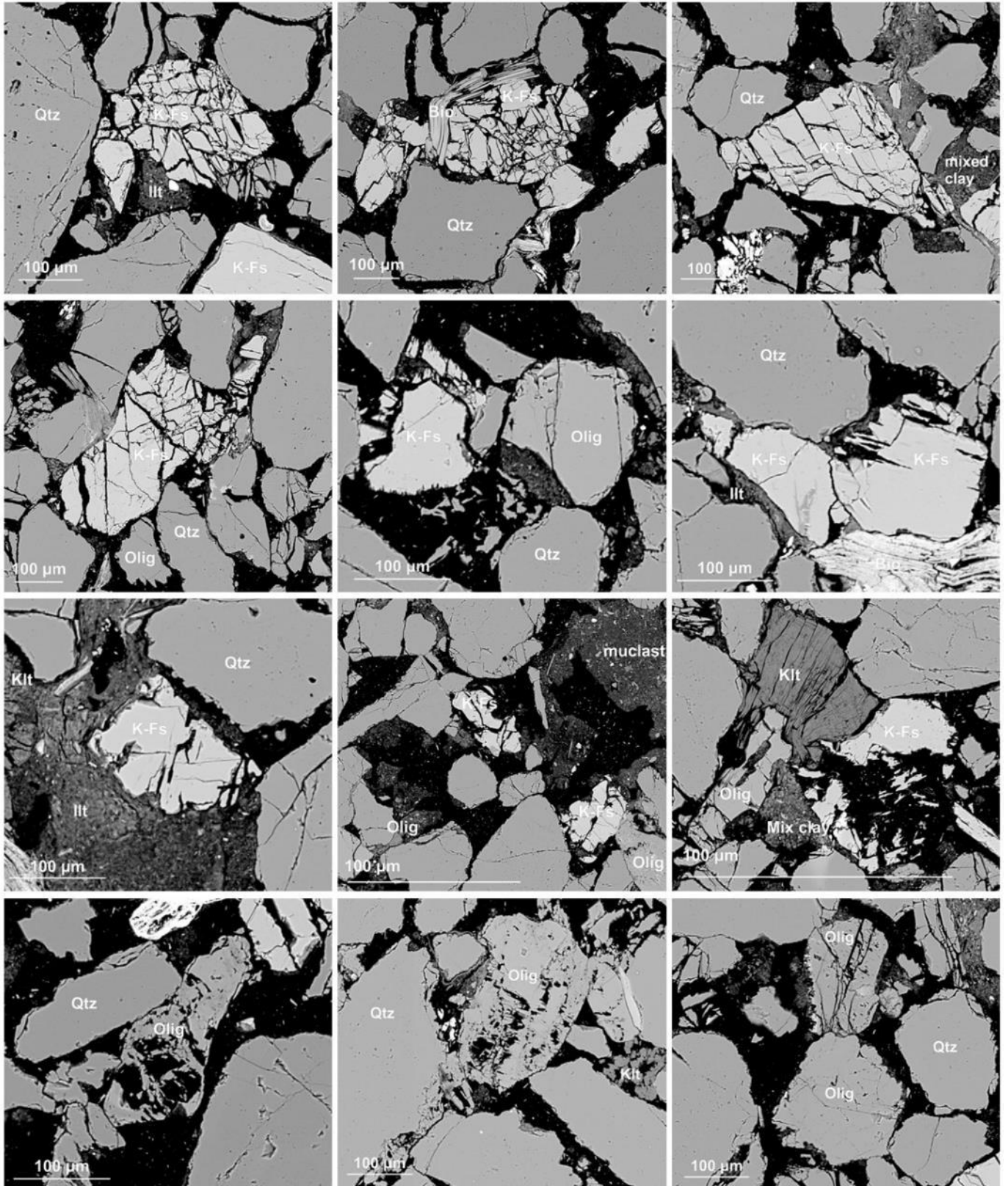


Figure S5. BSE images of sample Dt02, reacted with CO₂ fluids at 80°C. Larger K-feldspar (K-Fs) grains display fractures along semi-parallel intergranular fractures, likely reflecting structural weakening along cleavage planes, while smaller grains exhibit grain-edge cleavage cracks and partial dissolution. Secondary pores are commonly contain partially dissolved K-feldspar and some precipitates including illite (Illt).

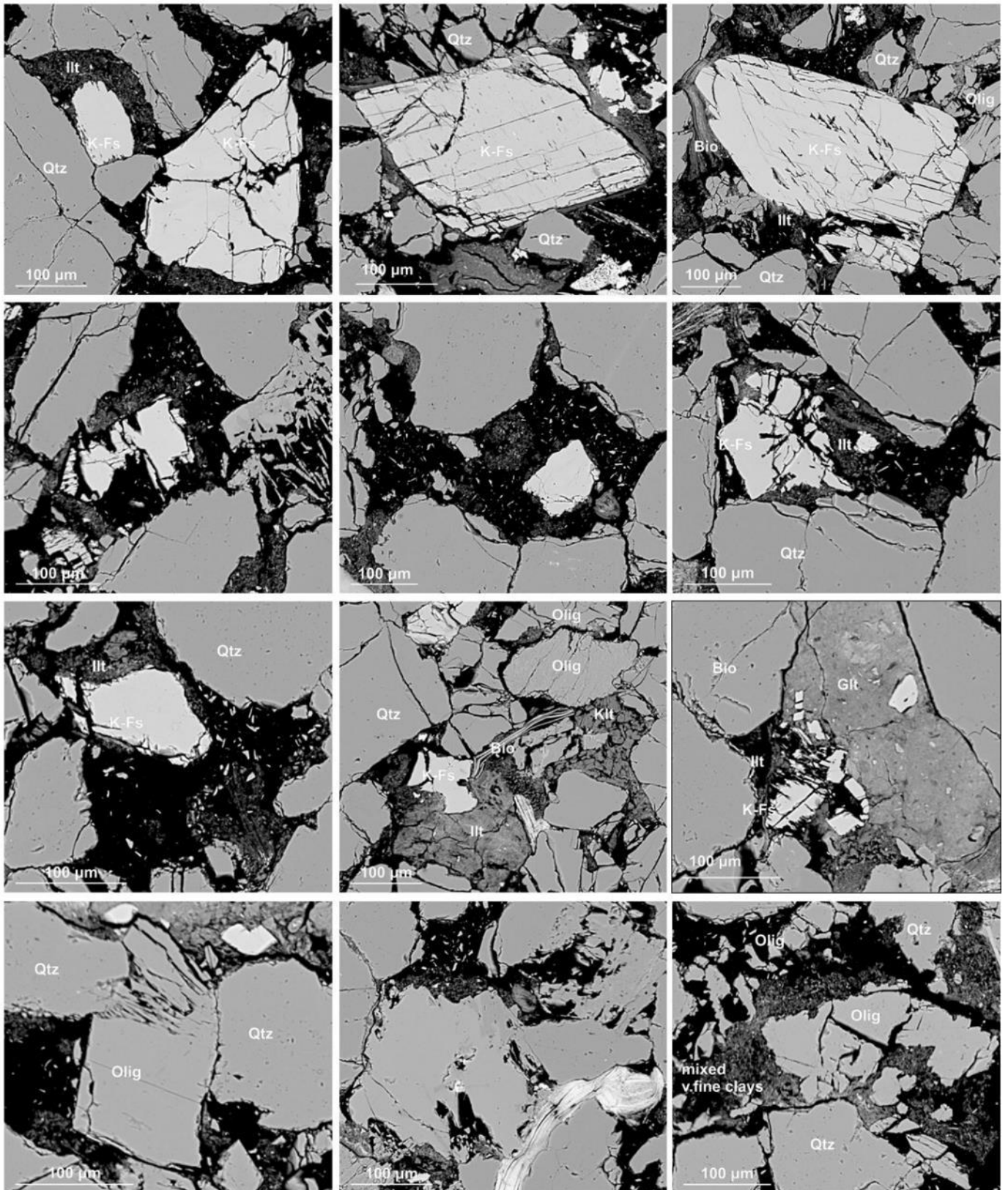


Fig S6. BSE images of sample DT01 reacted with CO₂ fluids at 250°C. Many K-feldspar (K-Fs) grains show dissolution along intergranular and grain-edge cleavage fractures. Secondary pores are commonly observed containing partially dissolved K-feldspar grains and illite (Ill).

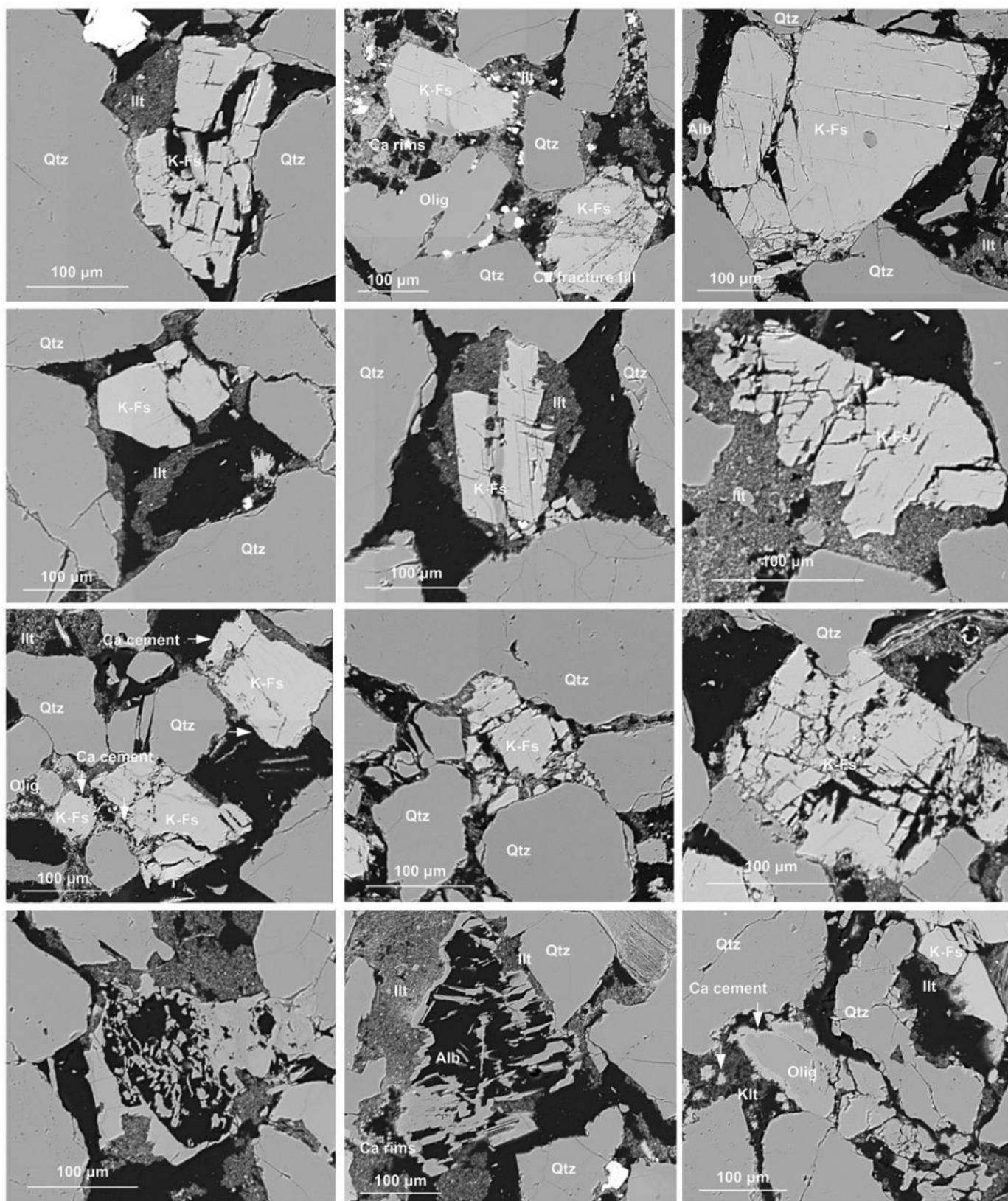


Fig S7. BSE images of sample DT03 reacted with CO₂ fluids at 400°C.

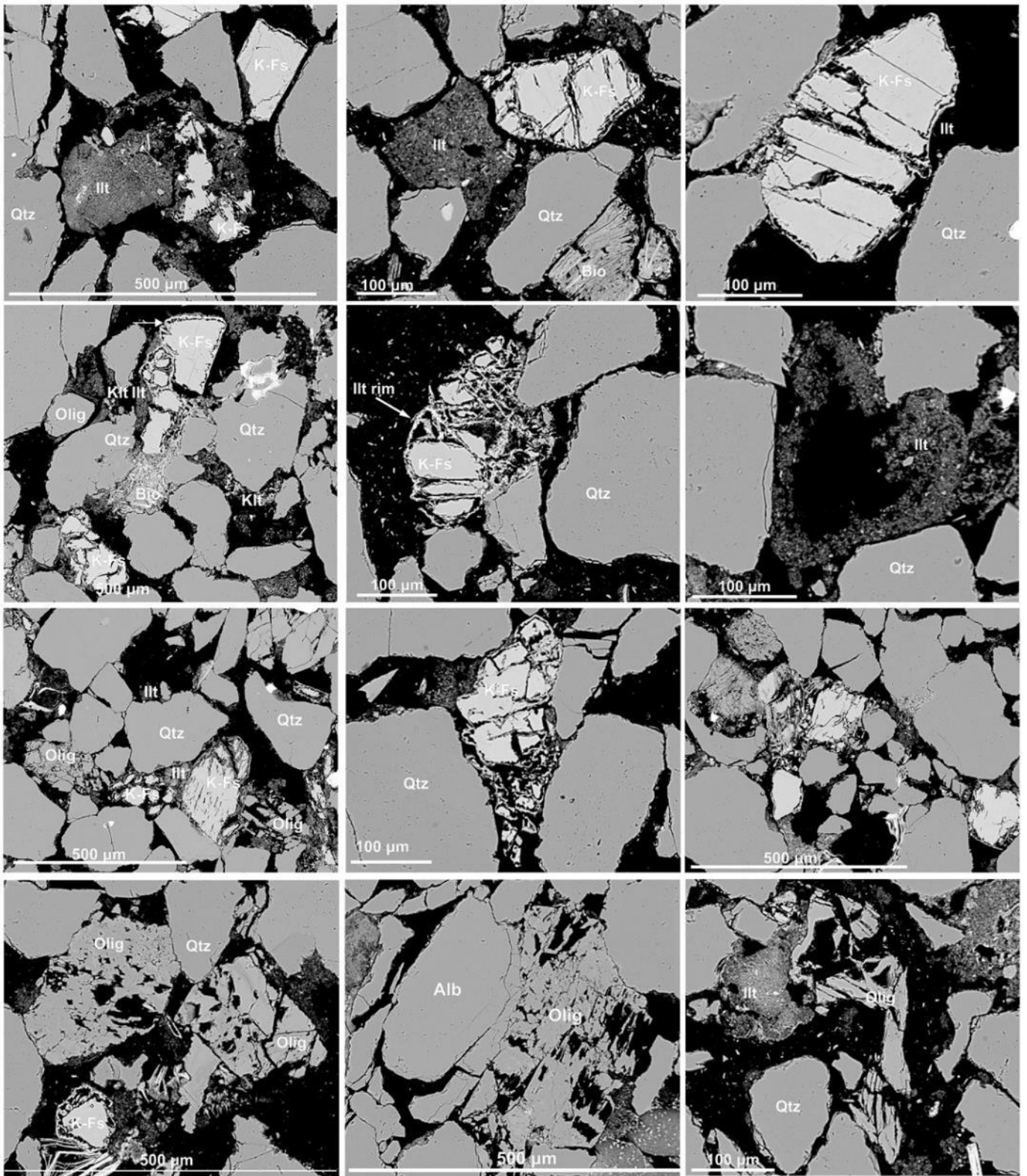


Fig S8. BSE images of sample DM05 reacted with CO₂ fluids at 550°C.

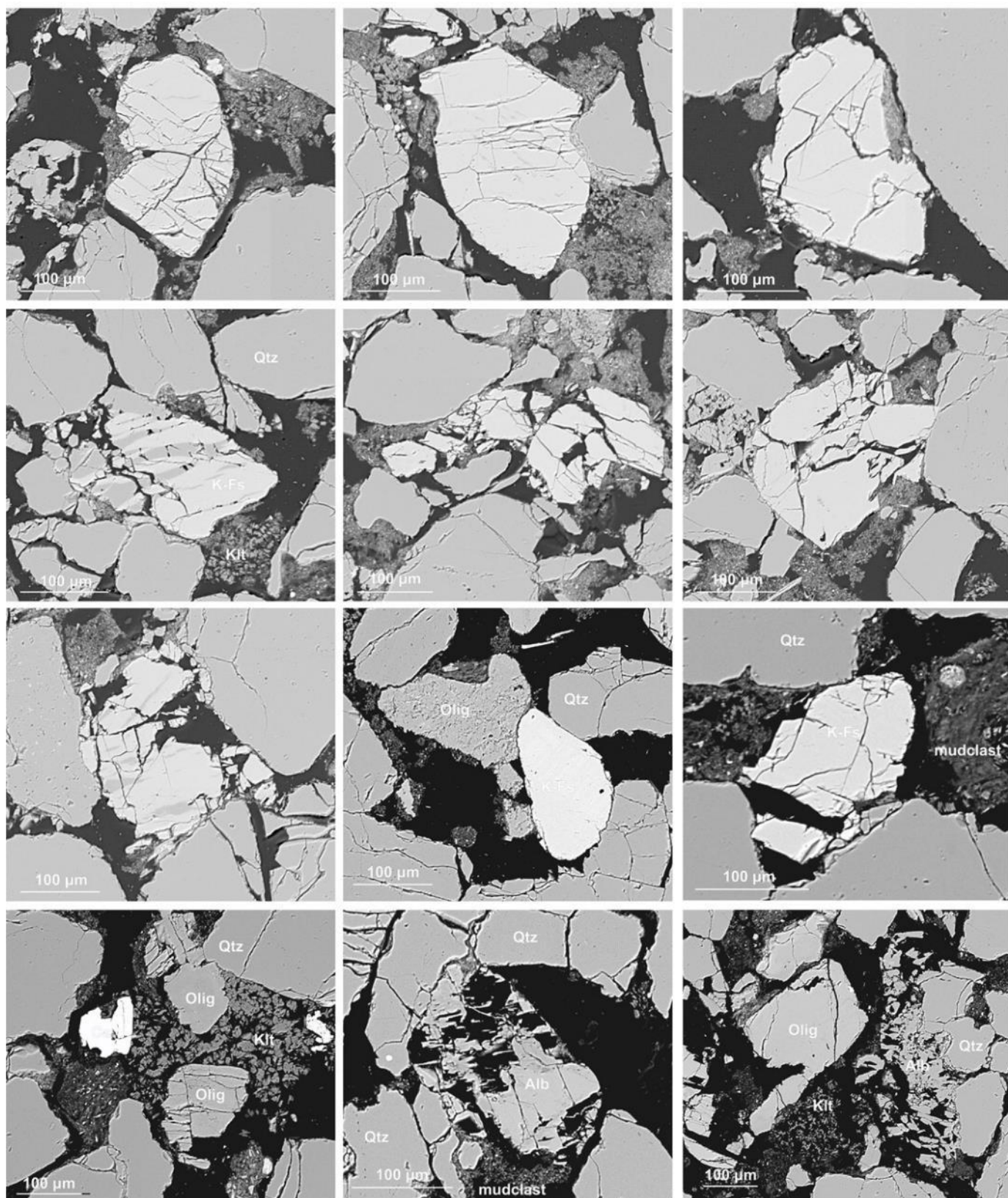


Fig S9. BSE images of sample Dm07 reacted with H₂O fluids at 80°C.

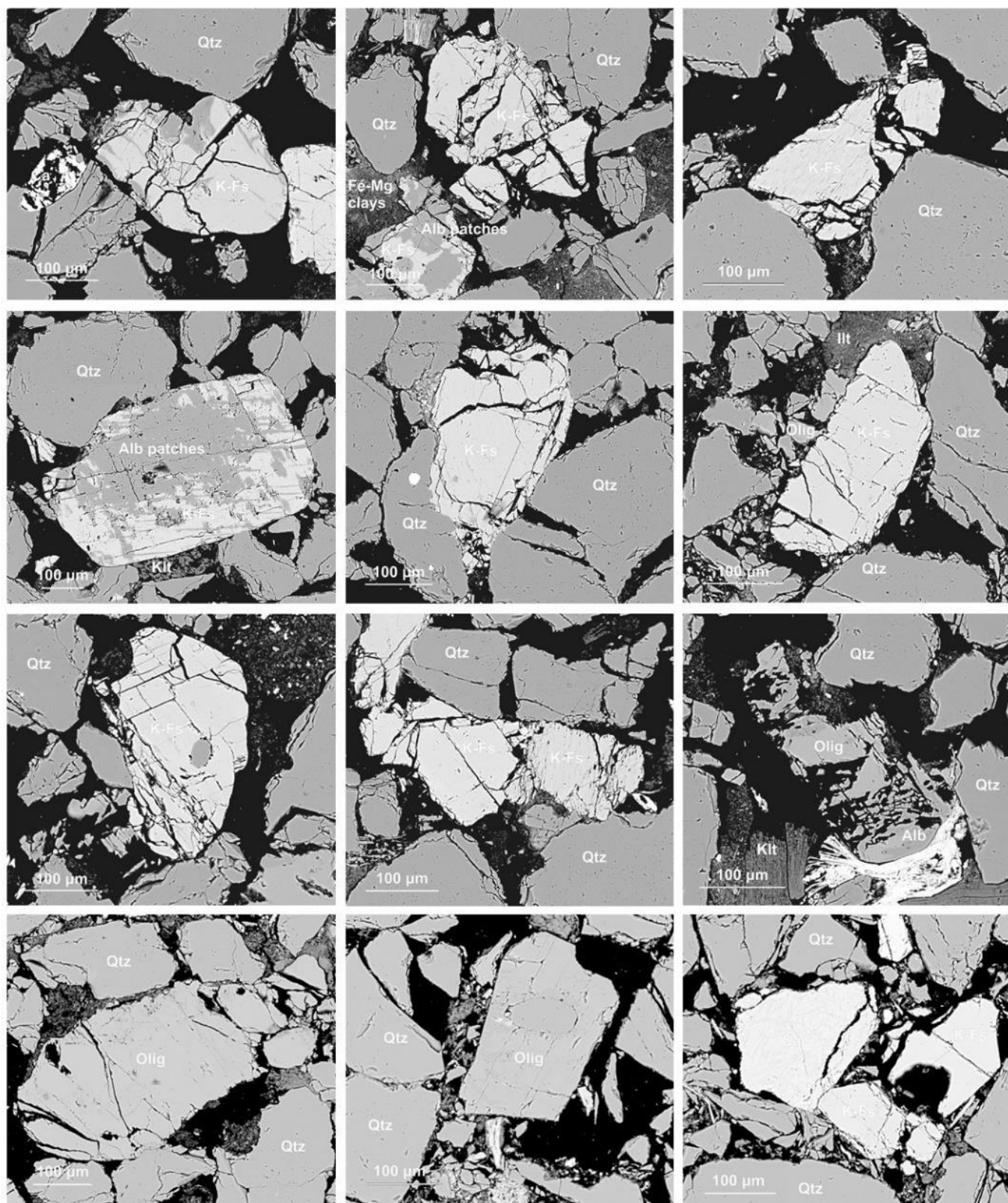


Fig S10. BSE images of sample Dm04 reacted with H₂O fluids at 250°C.

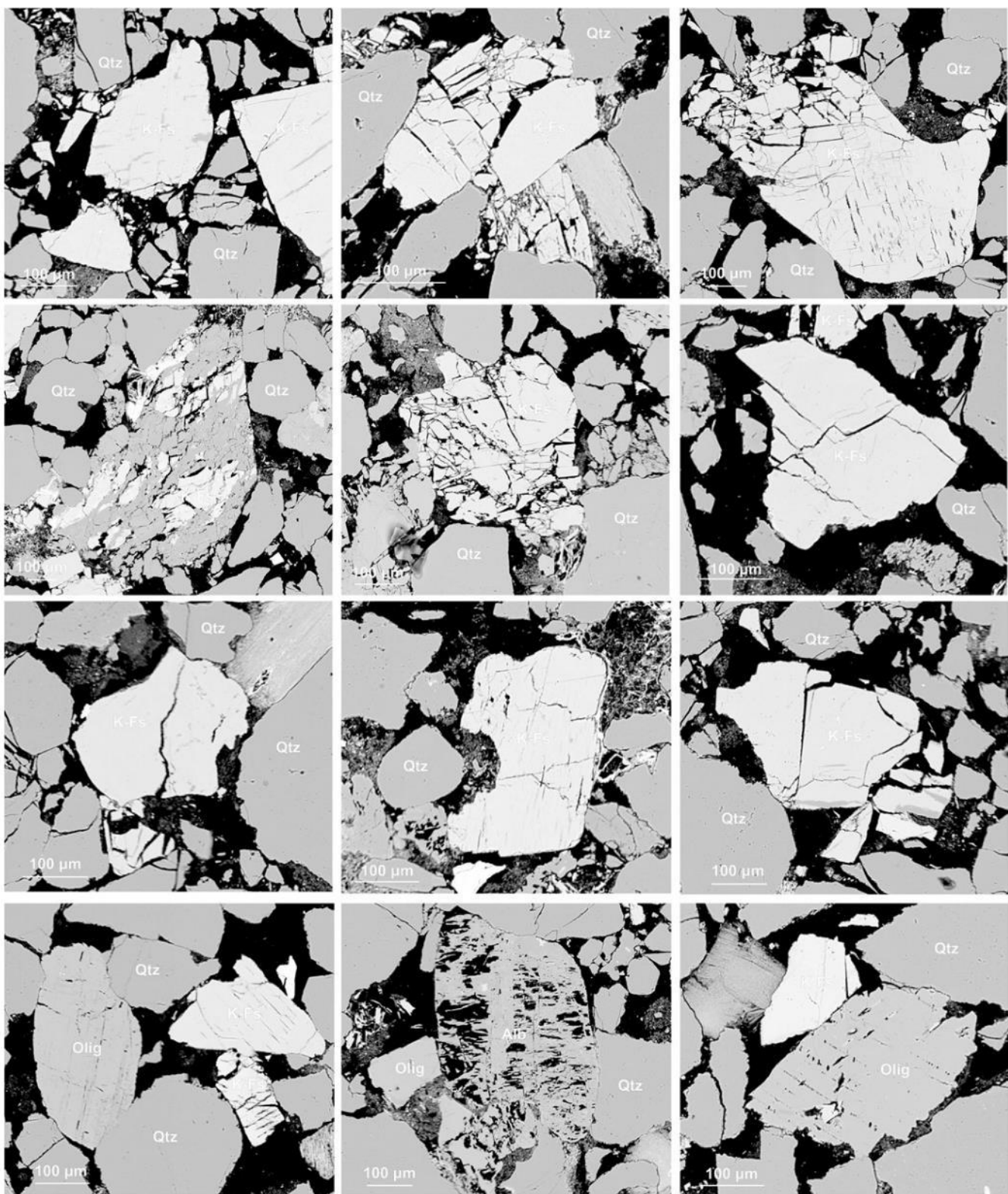


Fig S11. BSE images of sample Dm06 reacted with H₂O fluids at 400°C.

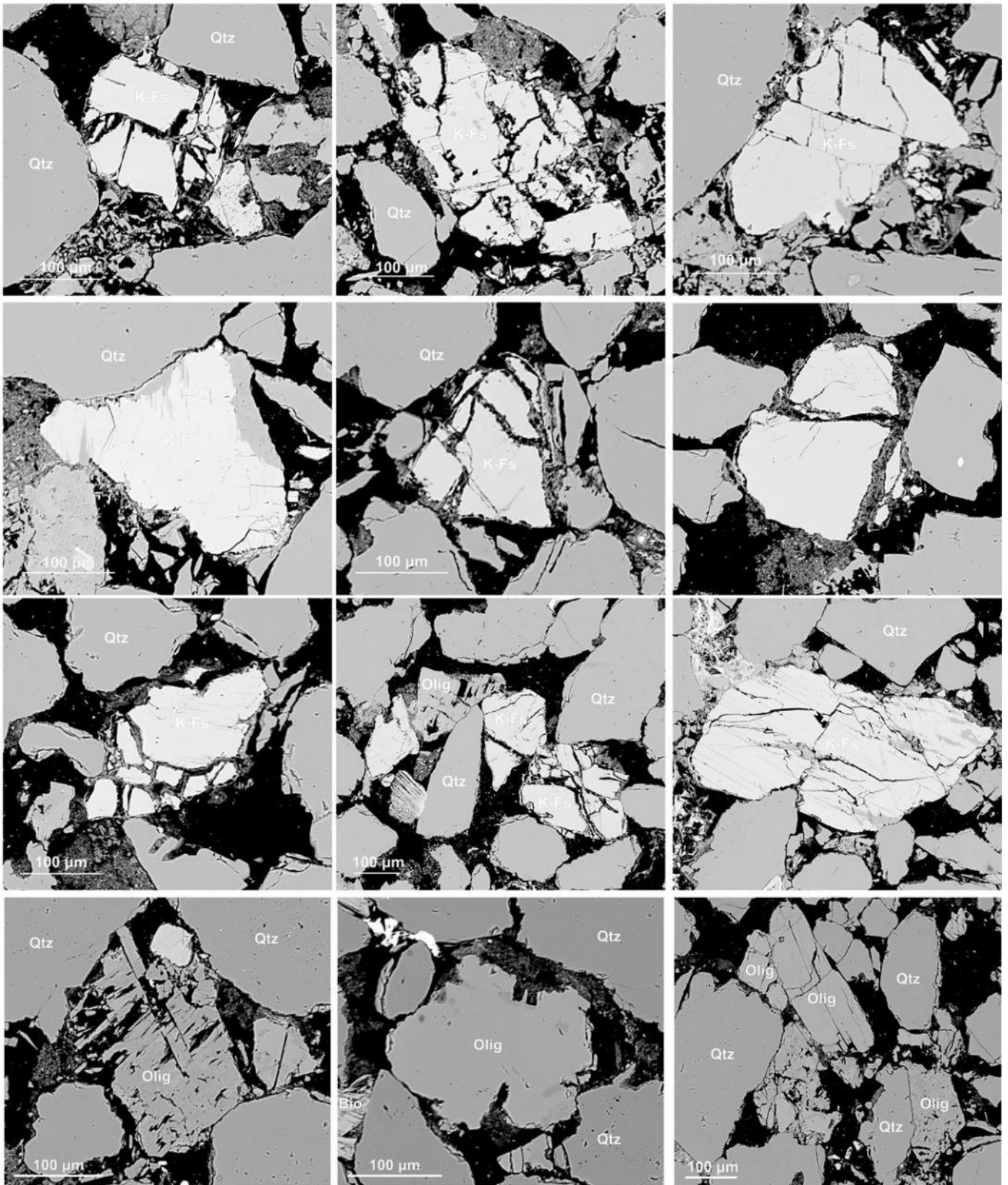


Fig S12. BSE images of sample Dm01 reacted with H₂O fluids at 550°C.

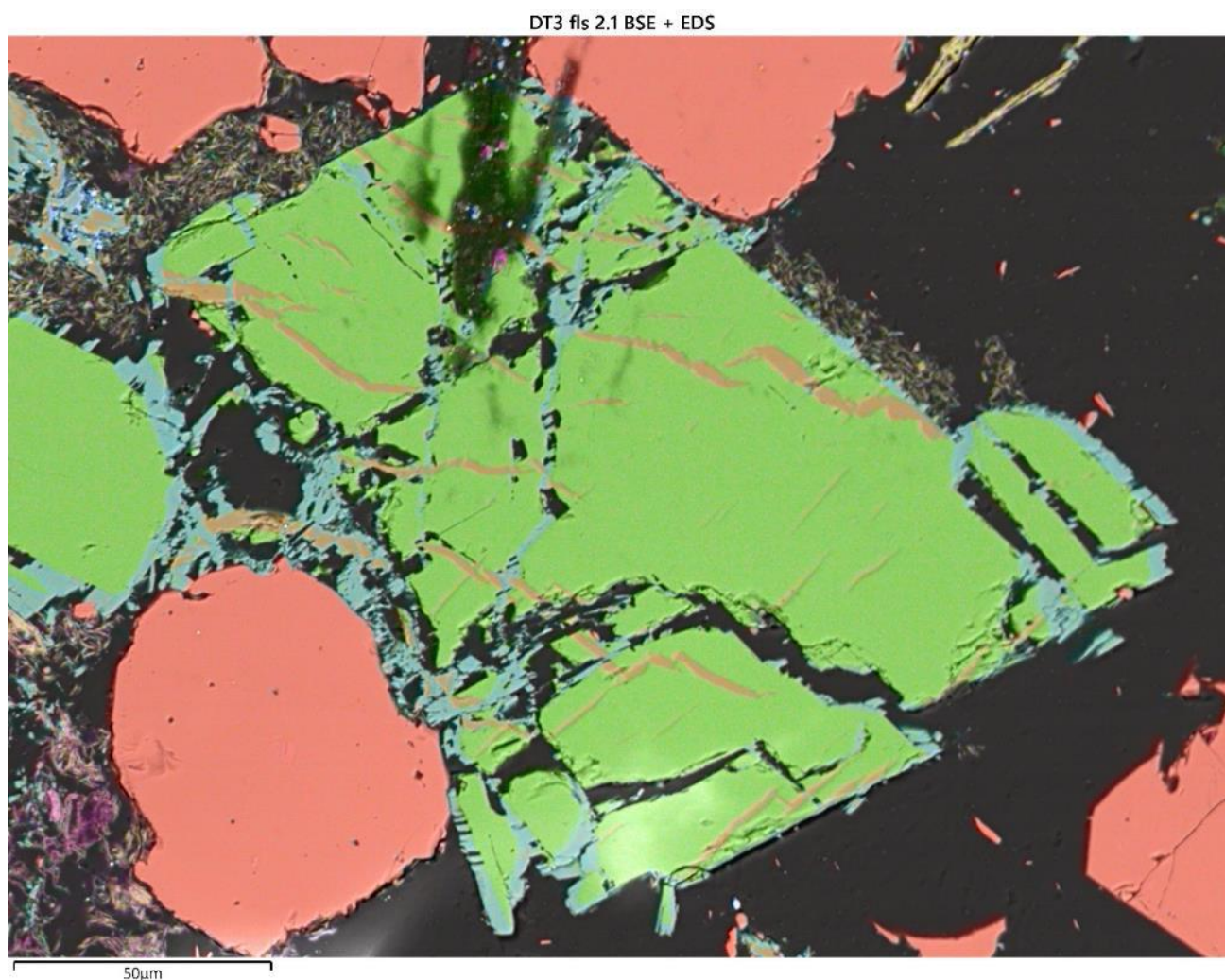


Fig S13. EDS BSE map of K-feldspar in post experimental sample DT03. In this image apparent anisotropic overgrowth of calcic aluminosilicates can be seen oriented from bottom left to top right of the image.

S2.2. FELDSPAR AND SECONDARY MINERAL COMPOSITIONS

Pre- and post-experimental feldspar compositions were determined using the SEM facility at CASP, as detailed in the main manuscript.

Pre-experimental compositions were extracted from a representative 7.5×7.5 mm representative large area map montages of the investigated DM and DT samples (<https://doi.org/10.6084/m9.figshare.30084970.v2>), using an accelerating voltage of 20 kV, a working distance of 8.5 mm, a probe current of approximately 2 nA and an EDS resolution of 1 μm. Using Oxford Instruments AZtec version 6.2, individual grains were traced to extract their composition and were calibrated using copper tape and Oxford Instruments “standardless” approach, as outlined by Pinard et al, (2020). A feldspar ternary plot (Fig 14) shows that the compositions are predominantly orthoclase, albite and oligoclase.

DM pre-experiment

DT pre-experiment

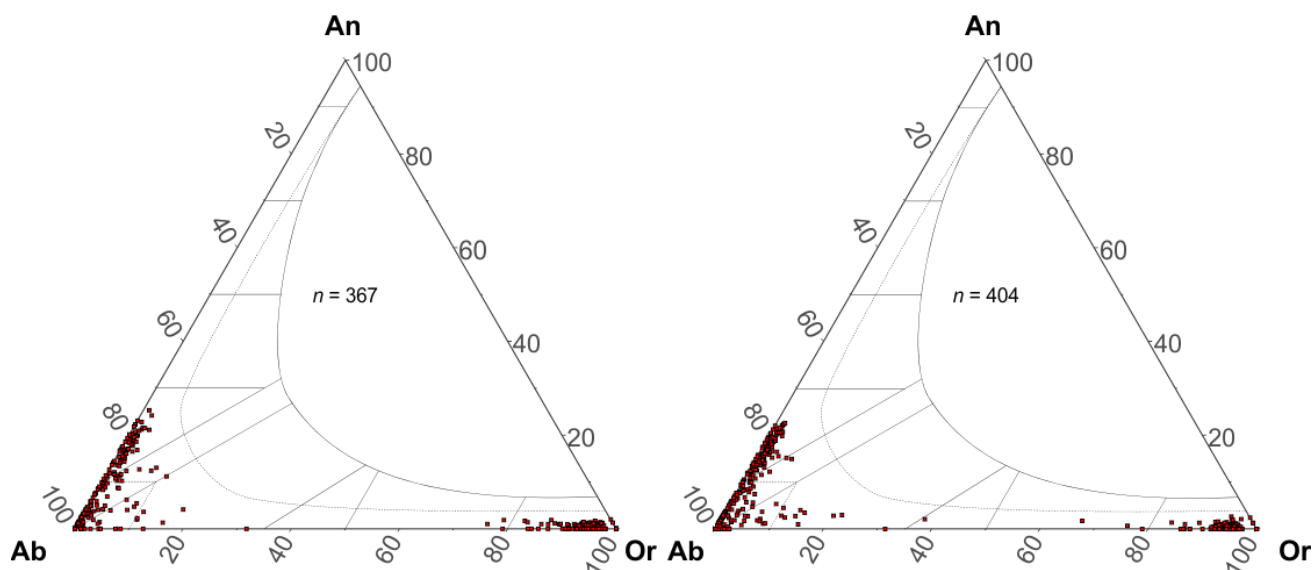


Figure S14. Ternary diagrams showing the composition of detrital feldspars for the pre-experimental DM and DT samples. Each point shows the average composition for a single detrital grain from a representative 7.5 mm² area.

Post-experimental analyses were determined using a spot analysis as follows: an accelerating voltage of 10 kV, a working distance of 8.5 mm and a probe current of approximately 2 nA. A mineral standard calibration was established using several phases in a MIN53-25 standard block (from Micro-Analysis Consultants Limited; Table 3), similar to the approach of Guyett et al. (2024). One million counts were collected per analysis by scanning over a rectangular area of <10 µm width at very high magnification. Beam intensity was calibrated using aluminium tape. Oxygen abundance was calculated from the stoichiometry. Labradorite from Tabor Island, Labrador, Canada, mounted in the MIN53-25 standard block was analysed intermittently as a secondary standard to confirm the veracity of the standard calibration and to monitor instrument drift (Table 4). The unnormalised sample data obtained are reported in excel file available at <https://doi.org/10.6084/m9.figshare.30084970.v2> and the positions of spot analyses are shown on BSE images (Figure 15). The feldspar ternary plot of post experiment samples shows that the compositions are generally more calcic (Figure 16).

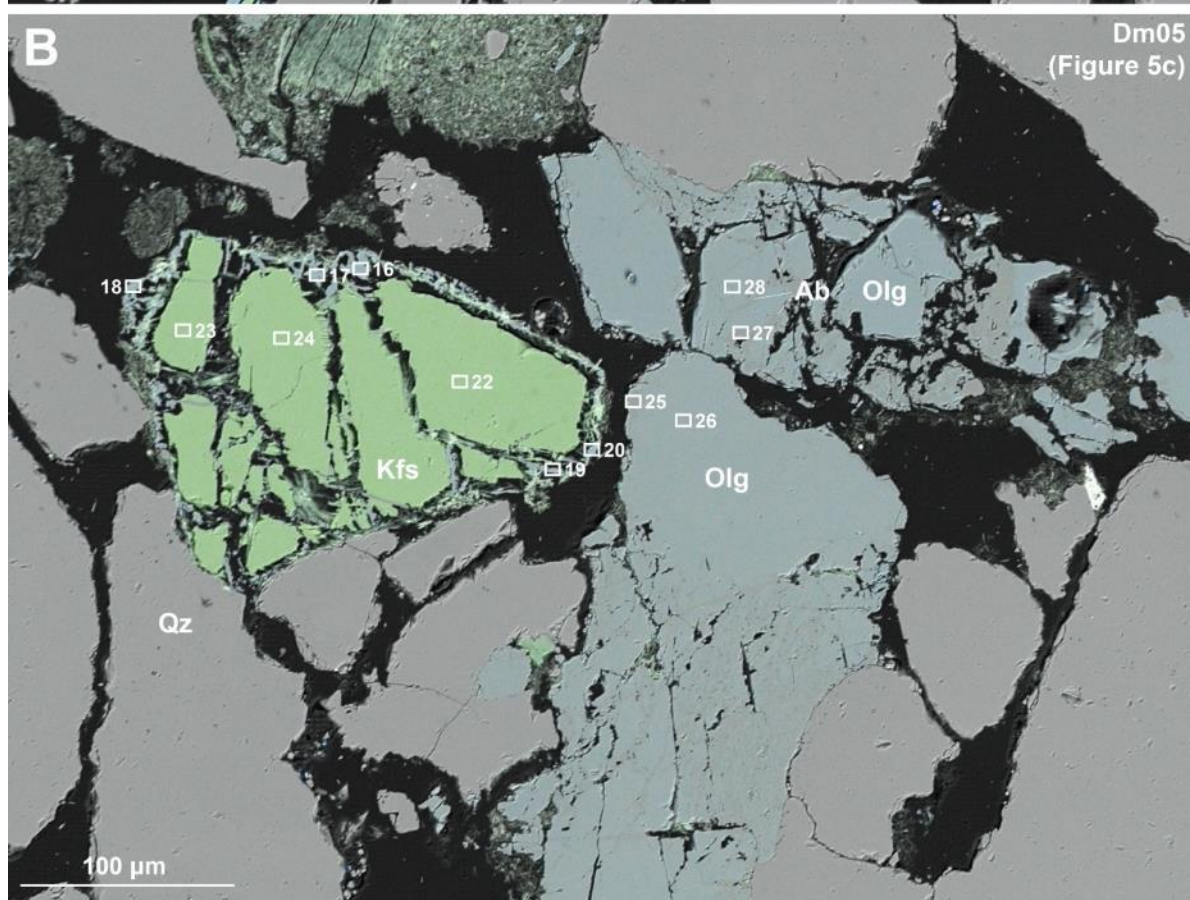
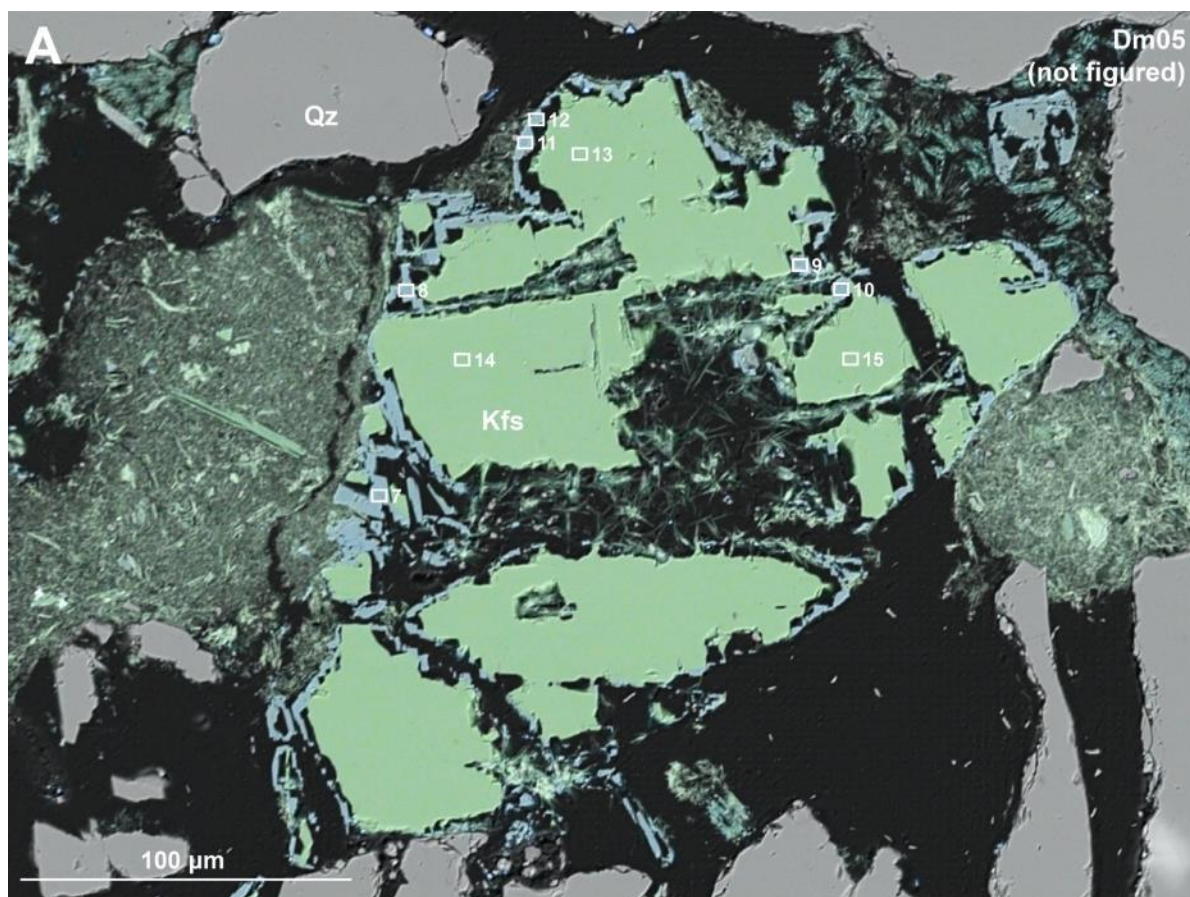
Element	Albite	Almandine	Diopside	Orthoclase	Benitoite	Celestine
O	48.78	40.33	43.72	46.72	34.51	35.03
Na	8.51		0.12	2.37		
Mg		3.46	10.3			
Al	10.54	11.47	0.38	10.16		
Si	31.93	17.48	25.16	30.54	19.8	
S						17.66
K	0.17			9.83		
Ca	0.07	1.11	17.84			
Ti			0.18		12.01	
Mn		0.93				
Fe		25.21	2.25			
Sr						46.65
Zr			0.06			
Ba				0.38	33.67	0.66

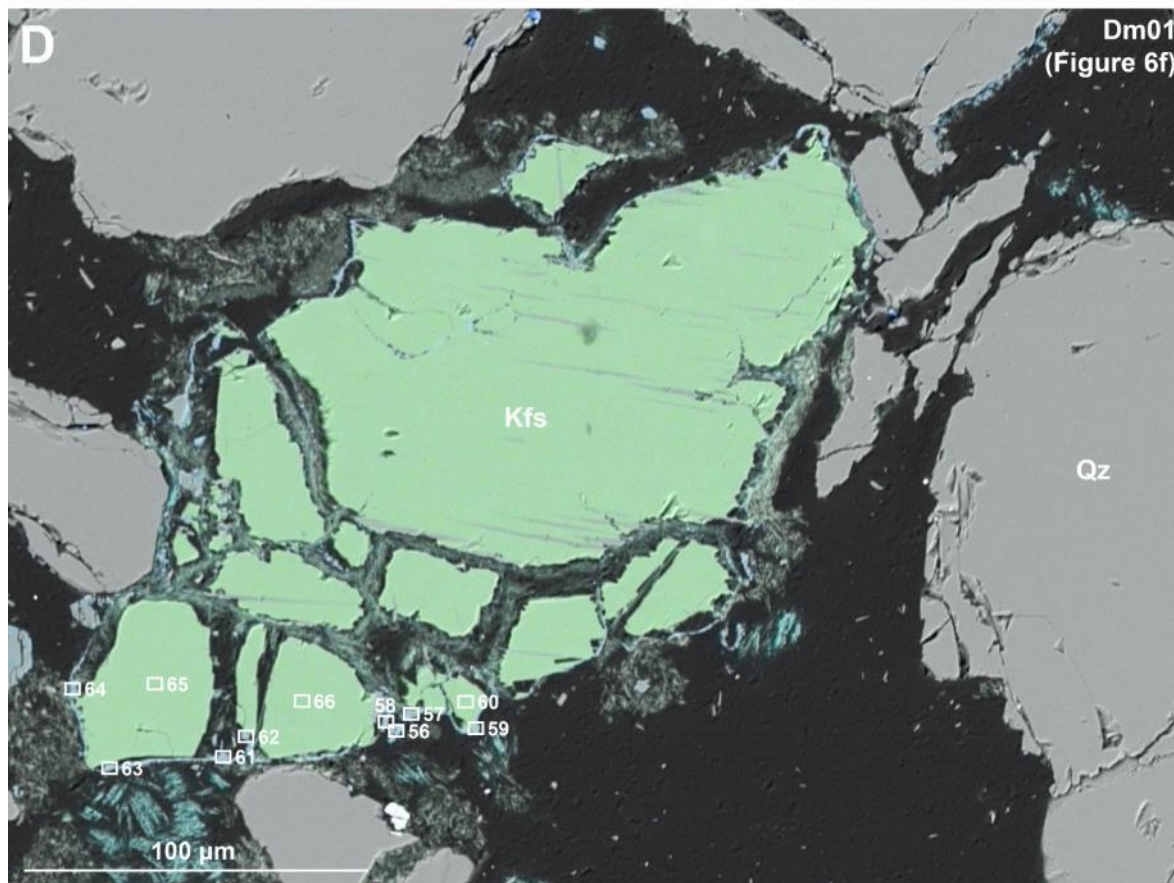
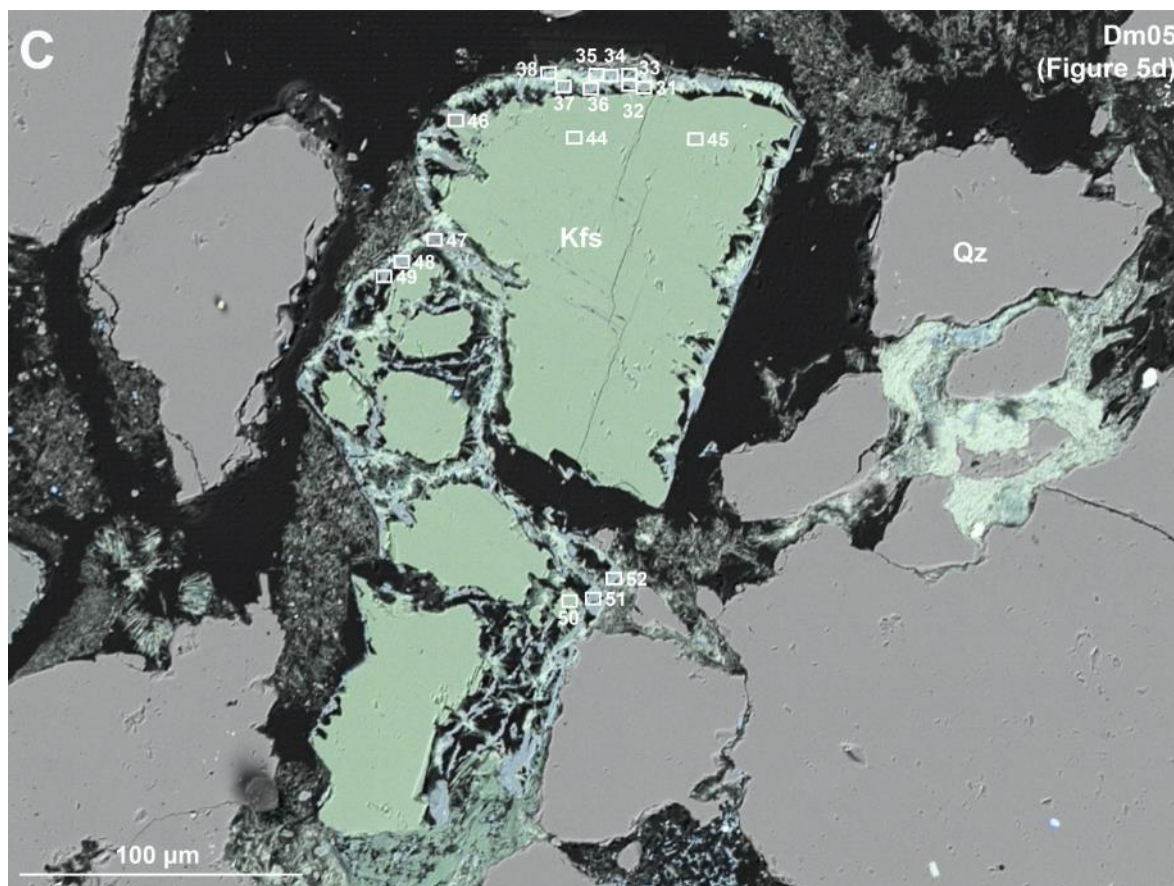
141 Table S3. Materials analysed from the MIN53-25 standard to supplement the factory standard calibration for the
142 spot analyses. Elements shown in bold were used in the calibration of sample analyses.

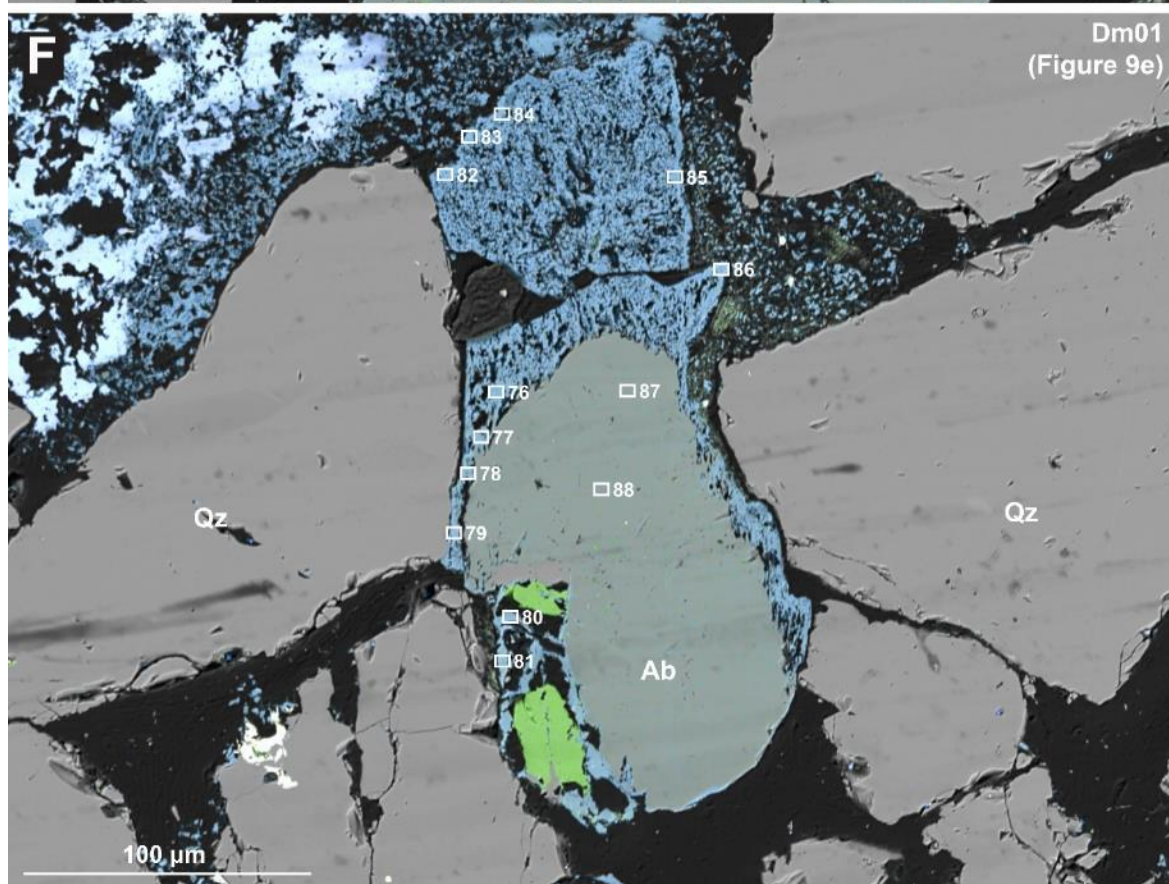
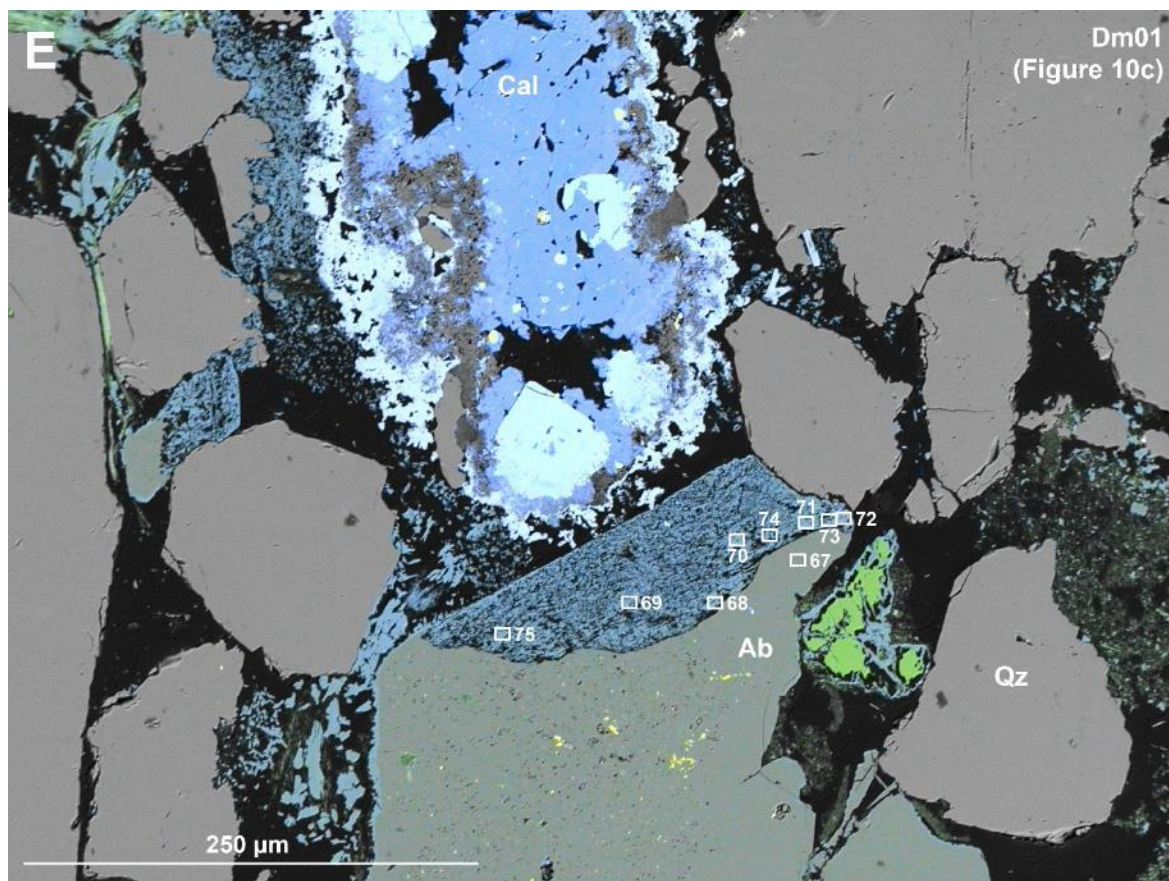
	Mean measured	2SE	Accepted average	2SE
O	47.32	0.15	47.18	0.03
Na	3.91	0.02	3.93	0.05
Al	14.85	0.05	14.87	0.05
Si	26.08	0.09	25.84	0.07
K	0.35	0.01	0.46	0.05
Ca	7.37	0.03	7.45	0.10
Fe	0.01	0.03	0.26	0.04

143 Table S4. SEM-EDS chemical data from labradorite in standard block MIN-53-25. Based on 16 analyses. *Note
144 that Fe was not resolvable from the background for most of the analyses undertaken and is consequently
145 underrepresented and inaccurate. SE = standard error.

146







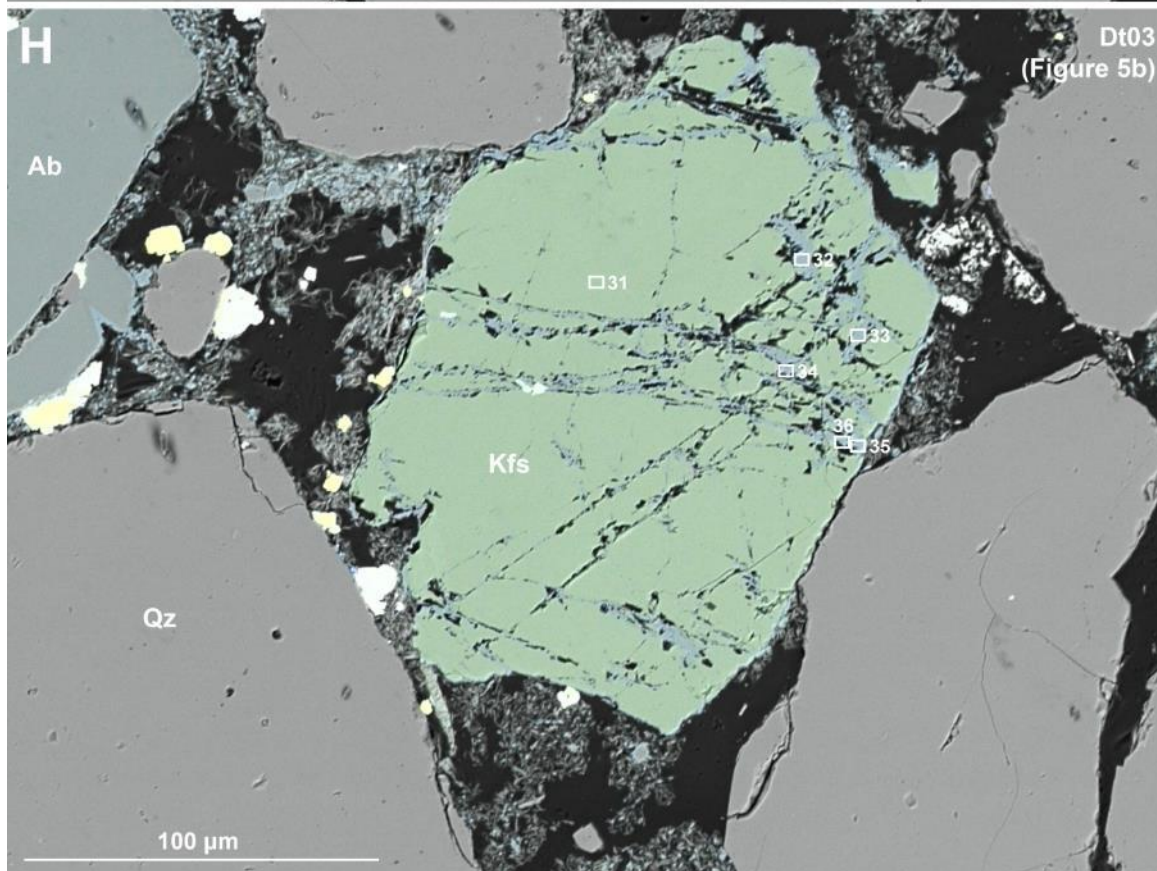
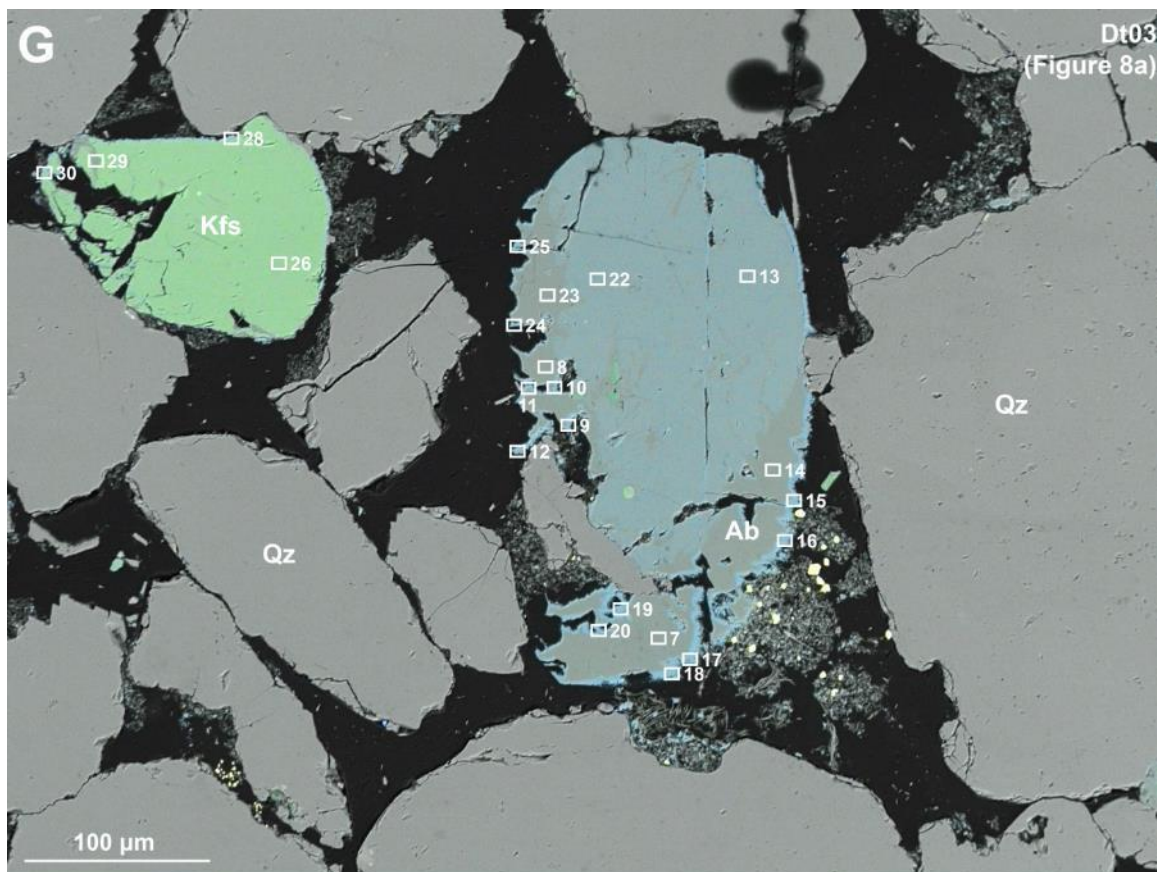


Fig S15. Continued overleaf.

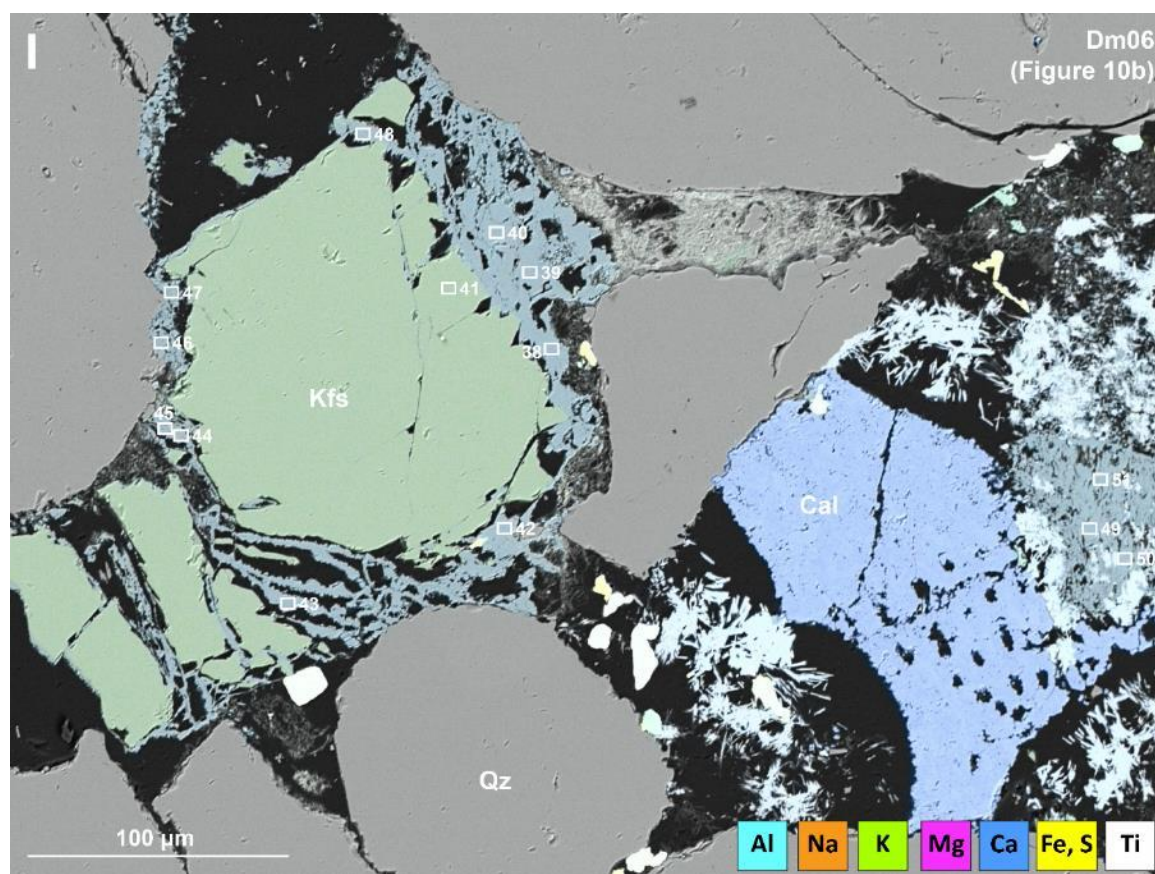


Fig S15. (A–I). BSE and semi-transparent EDS elemental maps showing the locations of feldspar spot analyses. All areas apart from A are figured in the main manuscript. The same elemental colours are used throughout.

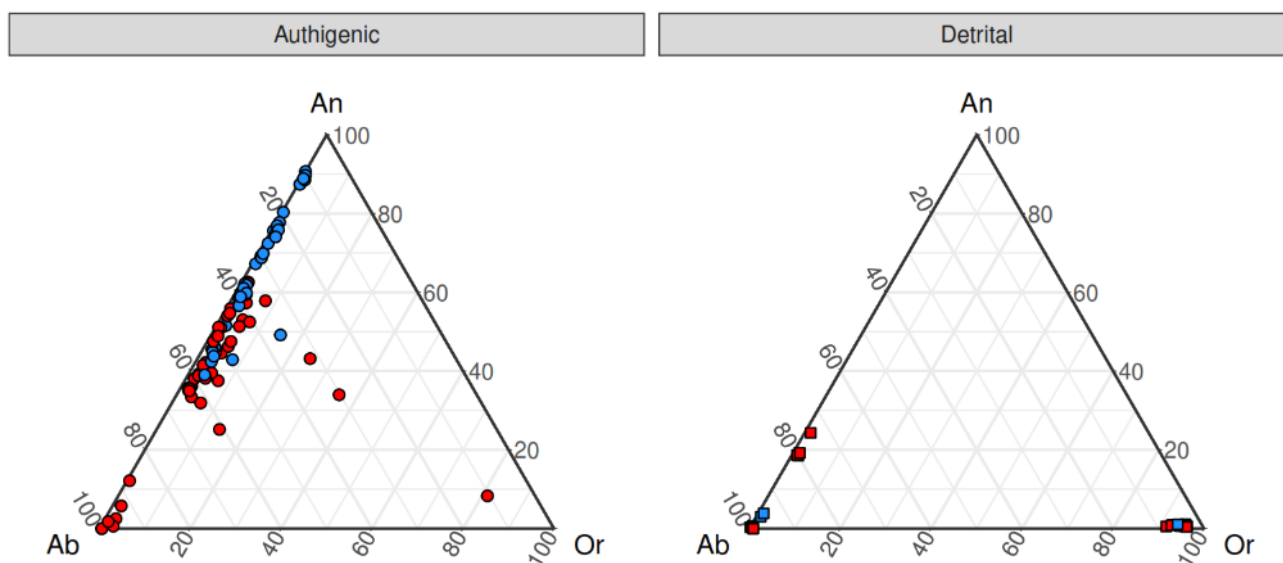


Figure S16. Ternary diagrams of feldspar compositions showing the new authigenic compositions and detrital grains, where red represents the CO₂ experiments and blue the H₂O experiments.

References

- Blum, A.E., Stilling, L. 1995. Feldspar dissolution kinetics. Chemical weathering rates of silicate minerals, pp.291-351.
- Guyett, P.C., Chew, D., Azevedo, V., Blennerhassett, L.C., Rosca, C. and Tomlinson, E., 2024. Optimizing SEM-EDX for fast, high-quality and non-destructive elemental analysis of glass. *Journal of Analytical Atomic Spectrometry*, 39(10), pp.2565-2579.
- Hall, M.R., Dim, P.E., Bateman, K., Rochelle, C.A. and Rigby, S.P., 2015. Post-CO₂ injection alteration of pore network geometry and intrinsic permeability of Permo Triassic sandstone reservoir". *Geofluids*, 10.1111/gfl. 12146.
- Helgeson, H.C., Murphy, W.M. and Aagaard, P., 1984. Thermodynamic and kinetic constraints on reaction rates among minerals and aqueous solutions. II. Rate constants, effective surface area, and the hydrolysis of feldspar. *Geochimica et Cosmochimica Acta*, 48(12), pp.2405-2432.
- Pinard P.T., Protheroe A., Holland J., Burgess S. and Statham P.J. (2020) Development and validation of standardless and standards-based X-ray microanalysis. *Materials Science and Engineering*, 891, 012020.
- Shell, 2015 'Peterhead CCS Project Doc Title: Geochemical Reactivity Report Doc No. PCCS-05-PT-ZR-3323-00001'. Available on Gov.UK website at [PVT Modelling Report for CO₂ in Goldeneye Project](#)

181 Whitney, D.L., Evans, B.W., 2010. Abbreviations for names of rock-forming minerals. Amer.
182 Mineral. 95, 185–187